Draft version September 13, 2016
Preprint typeset using LaTeX style AASTeX6 v. 1.0

arXiv:1609.02924v1 [astro-ph.CO] 9 Sep 2016

THE EFFECTS OF PHYSICALLY UNRELATED NEAR NEIGHBORS ON THE GALAXY-GALAXY LENSING SIGNAL

Tereasa G. Brainerd[1]
Department of Astronomy
Boston University
725 Commonwealth Avenue
Boston, MA 02215 USA

[1]brainerd@bu.edu

ABSTRACT

The effects of near neighbors on the galaxy-galaxy lensing signal are investigated using a suite of Monte Carlo simulations. The redshifts, luminosities, and relative coordinates for the simulated lenses were obtained from a set of galaxies with known spectroscopic redshifts and known luminosities. As expected, when all lenses are assigned a single, fixed redshift, the mean tangential shear is identically equal to the excess surface mass density, scaled by the critical surface mass density: $\gamma_T = \Delta\Sigma \times \Sigma_c^{-1}$. When the lenses are assigned their observed redshifts and Σ_c is taken to be the critical surface mass density of the central lens, the relationship $\gamma_T = \Delta\Sigma \times \Sigma_c^{-1}$ is violated because $\gtrsim 90\%$ of the near neighbors are located at redshifts significantly different from the central lenses. For a given central lens, physically unrelated near neighbors give rise to a ratio of γ_T to $\Delta\Sigma \times \Sigma_c^{-1}$ that spans a wide range of ~ 0.5 to ~ 1.5 at projected distances $r_p \sim 1$ Mpc. The magnitude and sense of the discrepancy between γ_T and $\Delta\Sigma \times \Sigma_c^{-1}$ are functions of both r_p and the velocity dispersions of the central lenses, σ_v. At large r_p, the difference between γ_T and $\Delta\Sigma \times \Sigma_c^{-1}$ is, on average, much greater for low-σ_v central lenses than it is for high-σ_v central lenses.

Keywords: dark matter — galaxies: halos — gravitational lensing: weak

1. INTRODUCTION

Galaxy galaxy lensing, the systematic weak lensing of background galaxies by foreground galaxies, is powerful method by which the amount of dark matter and its relationship to luminous matter can be directly constrained. The first statistically-significant ($\gtrsim 4\sigma$) detections of galaxy-galaxy lensing to be published in the peer-reviewed literature demonstrated the viability of galaxy-galaxy lensing as a cosmological tool, but the sample sizes of foreground and background galaxies were too small to place particularly strong constraints on the properties of the dark matter halos of the foreground galaxies (e.g., Brainerd et al. 1996; Dell'Antonio & Tyson 1996; Griffiths et al. 1996; Hudson et al. 1998). Later studies were able to take advantage of increasingly large samples, leading to improved constraints and demonstrating the importance of large surveys in the detection of the galaxy-galaxy lensing signal (e.g., Fischer et al. 2000; Guzik & Seljak 2002; Hoekstra et al. 2004, 2005; Sheldon et al. 2004; Mandelbaum et al. 2005, 2006; Heymans et al 2006; Kleinheinrich et al. 2006; Tian et al. 2009). More recently, increasingly large data sets from the Sloan Digital Sky Survey (York et al. 2000), the Dark Energy Survey (Flauger 2005), the COSMOS survey (Koekemoer et al. 2007; Scoville et al. 2007ab), the Red Sequence Cluster Survey 2 (Gilbank et al. 2011), the Canada-France-Hawaii Telescope Lensing Survey (Heymans et al. 2012; Erben et al. 2013), and the combination of the Galaxy And Mass Assembly Survey (Driver et al. 2009, 2011; Liske et al. 2015) with the Kilo Degree Survey (Kuijken et al. 2015) have continued to dramatically improve the constraints that can be placed on the relationship between dark and luminous matter from galaxy-galaxy lensing. These most recent studies have placed strong constraints on the stellar-to-halo mass relation, the luminosity-to-halo mass relation, the dependence of the average halo mass on cosmic environment, and the masses of the halos surrounding passive versus star-forming galaxies (e.g., van Uitert et al. 2011, 2015, 2016; Leauthaud 2012ab; Tinker et al. 2013; Brimioulle et al. 2013; Velander et al. 2014; Coupon et al. 2015; Hudson et al. 2015; Zu & Mandelbaum 2015; Brouwer et al. 2016; Clampitt et al. 2016; Mandelbaum et al. 2016).

A key goal for galaxy-galaxy lensing studies is a measurement of the surface mass density surrounding central lens

galaxies via observations of the mean tangential shear, $\gamma_T(r_p)$. In the case of isolated, axisymmetric lenses, it is well-known that the mean tangential shear is related to the excess surface mass density, $\Delta\Sigma(r_p)$, through

$$\Delta\Sigma(r_p) \equiv \langle\Sigma(< r_p)\rangle - \Sigma(r_p) = \Sigma_c\ \gamma_T(r_p) \tag{1}$$

where $\langle\Sigma(< r_p)\rangle$ is the mean interior surface mass density contained within a circle of radius r_p, centered on the lens, and $\Sigma(r_p)$ is the surface mass density at radius r_p from the lens (e.g., Miralda-Escudé 1991). The quantity Σ_c is known as the critical surface mass density and is given by

$$\Sigma_c = \frac{c^2}{4\pi G}\frac{D_s}{D_l D_{ls}} \tag{2}$$

where G is Newton's gravitational constant, c is the velocity of light, D_l is the angular diameter distance between the observer and the lens, D_s is the angular diameter distance between the observer and the source, and D_{ls} is the angular diameter distance between the lens and the source. Equation 1 is also true in the case of an isolated non-axisymmetric lens so long as $\gamma_T(r_p)$ and $\Sigma(r_p)$ are interpreted as mean values, averaged over a ring of radius r_p, centered on the lens (see, e.g., Schneider 2006).

In the case of multiple lens galaxies that all share the same redshift (as would be the case for, say, the halos of satellite galaxies that are contained within a larger system), Equation 1 is also strictly true. It is this latter property of Equation 1 that is commonly used to convert an observed value of the mean tangential shear into a constraint on the excess surface mass density in galaxy-galaxy lensing studies. Since the value of Σ_c for a given lens-source pair depends upon the redshifts of both the lens and the source, the conversion of the shear into a constraint on the excess surface mass density requires a computation of the value of Σ_c that is appropriate for the sample. This is sometimes done by computing a mean value of Σ_c for the entire sample, and the mean is computed over the full lens-source distribution in redshift space. In that case, the right hand side of Equation 1 is evaluated as the product of the mean tangential shear, computed over all lens-source pairs, and the mean value of Σ_c. More often, a value of Σ_c is computed for each lens-source pair, then the products of the individual values of Σ_c and γ_T for each lens-source pair are averaged together to infer the mean excess surface mass density. Note that, in practice, various weighting schemes are typically used in observational studies in order to optimize the detection of the weak lensing shear and the reader is referred to recent papers on this subject for examples of these weighting schemes (see, e.g., Velander et al. 2014; Hudson et al. 2015; Brouwer et al. 2016).

The published observational constraints on $\Delta\Sigma(r_p)$ have all acknowledged that, in addition to shear caused by the central lens galaxies around which $\gamma_T(r_p)$ is computed (the so-called "one-halo" term), there is an additional contribution to $\gamma_T(r_p)$ at large r_p due to neighboring galaxies (the so-called "two-halo" term). For the most part, the two-halo term has been interpreted as being caused by neighboring galaxies that are physically associated with the central lens galaxies. That is, it is generally assumed that the two-halo term is dominated by neighboring galaxies that share the same redshift as the central lens galaxies (see, e.g., the review by Mandelbaum 2015). In the case that the two-halo term is, indeed, dominated by physically associated near neighbor galaxies, then Equation 1 can be used to infer the excess surface mass density directly from the observed mean tangential shear, with Σ_c being the value of the critical surface mass density that is appropriate for a given central lens, its physically associated near neighbors, and a given background source.

It is, however, not necessarily the case that the two-halo term is dominated by physically associated near neighbors. The first simulations of galaxy-galaxy lensing showed that, for a given lens galaxy, the closest lens on the sky was not necessarily the most important lens and, typically, a given source was lensed at a comparable level by at least 3 or 4 physically unrelated foreground galaxies (Brainerd et al. 1996). Additionally, Brainerd (2010) showed that, for a realistic population of lens galaxies with median redshift $z_{\rm med} = 0.55$, a population of source galaxies with median redshift $z_{\rm med} = 0.96$ would experience a significant amount of weak lensing due to multiple, physically unassociated galaxies.

The goal of this paper is to examine the degree to which physically unassociated near neighbors affect the galaxy-galaxy lensing signal in the limit of a realistic, relatively deep sample of lens galaxies. Using a set of galaxies with known spectroscopic redshifts and known luminosities, a suite of Monte Carlo simulations of galaxy-galaxy lensing were constructed using a simple, analytic dark matter halo model. From the simulations, the relationship between the mean tangential shear and the actual surface mass density can be investigated directly, and the net effects of multiple, physically unassociated lens galaxies on the galaxy-galaxy lensing signal can be assessed straightforwardly.

The paper is organized as follows. Details of the galaxy-galaxy lensing simulations are discussed in Section 2, and results for the mean tangential shear and the excess surface mass density, scaled by the critical surface mass density, are

presented in Section 3. A summary and discussion of the results are presented in Section 4. Throughout, the present-day values of the cosmological parameters are taken to be $\Omega_0 = 0.25$, $\Omega_{\Lambda 0} = 0.75$, and $H_0 = 70$ km sec^{-1} Mpc^{-1}.

2. SIMULATIONS OF GALAXY-GALAXY LENSING

To ensure the greatest realism in the simulations, relatively bright galaxies with known redshifts and known rest-frame blue luminosities (L_B) were selected from a region of diameter $4'$, centered on the Hubble Deep Field-North (HDF-N; Williams et al. 1996). This region of sky was the subject of both a deep redshift survey (Cohen et al. 1996; Steidel et al. 1996; Lowenthal et al. 1997; Phillips et al. 1997; Cohen et al. 2000) and an extensive multicolor photometric investigation (Hogg et al. 2000). For this investigation, the redshifts of the galaxies were obtained from Tables 2A and B from Cohen et al. (2000) and their rest-frame blue luminosities were obtained from Table 1 of Cohen (2001).

The completeness limits of the redshift survey differ for the HDF-N itself and the regions that surround it, with the completeness limit being shallower in the surrounding regions than it is in the HDF-N. In order assess the effects of near neighbors on the galaxy-galaxy lensing signal, however, it is important that the redshift distributions of the lenses be the same within both the HDF-N and the surrounding regions. Therefore, for this investigation a conservative completeness limit of $R = 23$ was imposed, resulting in the selection of 427 galaxies from Cohen et al. (2000) and Cohen (2001). The observed celestial coordinates, redshifts, and rest-frame blue luminosities of these galaxies were then used as the basis of a suite galaxy-galaxy lensing simulations in which the effects of differing numbers of near neighbors on the net mean tangential shear could be assessed directly. The advantage to using these particular galaxies for the simulations is that the relative lensing strengths of the galaxies are effectively known, since both the redshifts and the relative depths of the dark matter potential wells of the galaxies are known.

This investigation is not focussed on an accurate reproduction of an observed galaxy-galaxy lensing signal (i.e., such as one would want for the purpose of constraining the physical properties of the dark matter halos of the lens galaxies). Instead, here the focus is a demonstration of the net effect of near neighbor galaxies on the galaxy-galaxy lensing signal. Because of this, the simulations do not incorporate the contribution of all galaxies within this region of space to the galaxy-galaxy lensing signal. Rather, the simulations are restricted to the effects of, at most, the four nearest neighbors. The angular separations between each central lens galaxy and its near neighbors are denoted by θ_1, θ_2, θ_3, and θ_4, where θ_1 is the separation between a central lens galaxy and its nearest neighbor, θ_2 is the separation between a central lens galaxy and its second nearest neighbor, etc. In order to avoid edge effects that would be caused by not including weak lensing due to galaxies that are located just outside the region of the redshift survey, only those galaxies that are farther than $(4' - \theta_4)$ from the edge of the survey are selected as central lenses. A total of 348 galaxies with $R \leq 23$ are located sufficiently far from the edge of the survey to be selected as central lenses.

For simplicity, the dark matter halos of all galaxies were modeled as singular isothermal spheres, for which the surface mass density is given by

$$\Sigma(\theta) = \frac{\sigma_v^2}{2GD_l\theta}. \tag{3}$$

The Einstein radius of a singular isothermal lens is given by

$$\theta_E = 4\pi \left(\frac{\sigma_v}{c}\right)^2 \frac{D_{ls}}{D_s}, \tag{4}$$

and the shear for a singular isothermal lens is given by

$$\gamma(\theta) = \frac{\theta_E}{2\theta}. \tag{5}$$

Here σ_v is the velocity dispersion of the dark matter halo surrounding the lens galaxy and θ is the angular separation on the sky between the lens and the source. While this halo mass distribution is unphysical, it has the advantage of being both analytic and simple, allowing the results presented here to be reproduced both easily and straightforwardly.

Velocity dispersions for the halos of the galaxies were assigned using a simple Tully-Fisher or Faber-Jackson type of relation:

$$\frac{\sigma_v}{\sigma_v^*} = \left(\frac{L_B}{L_B^*}\right)^{1/4} \tag{6}$$

where σ_v^* is the velocity dispersion of the halo of a galaxy with rest-frame blue luminosity L_B^*. For the simulations presented here, a value of $\sigma_v^* = 156$ km sec^{-1} was adopted.

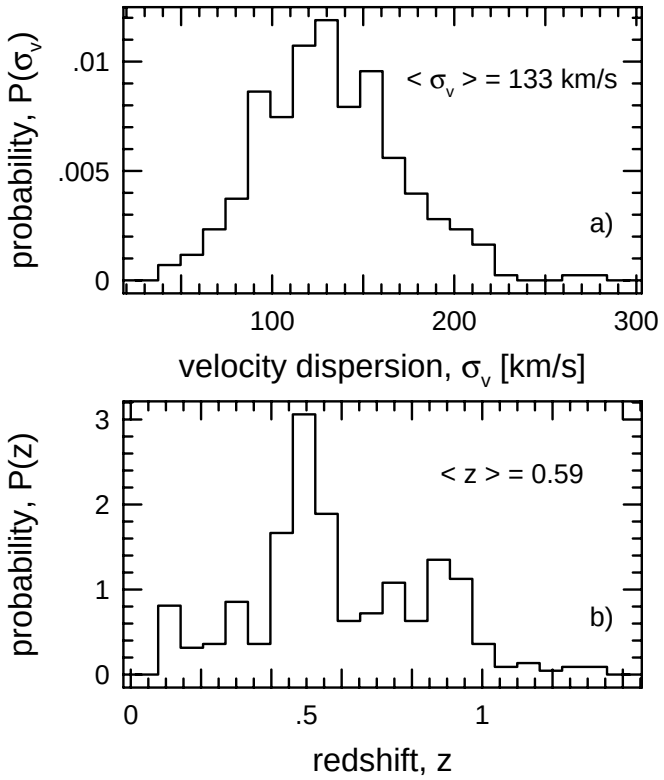

Figure 1. *Top:* Probability distribution for the velocity dispersions of the 348 central lens galaxies. Mean lens velocity dispersion is $\langle \sigma_v \rangle = 133$ km sec^{-1}. *Bottom:* Probability distributions for the redshifts of the 348 central lens galaxies. Mean lens redshift is $\langle z \rangle = 0.59$.

The distribution of velocity dispersions for the halos of the 348 central lens galaxies is shown in the top panel of Figure 1. The bottom panel of Figure 1 shows the redshift distribution for the 348 central lens galaxies. From Figure 1, the mean halo velocity dispersion for the central lenses is $\langle \sigma_v \rangle = 133$ km sec^{-1} and the mean redshift is $\langle z \rangle = 0.59$. The panels in Figure 2 show the distributions of a) halo velocity dispersion, b) redshift, c) absolute redshift difference relative to the central lens, and d) angular separation between the central lens and the galaxies that constitute the "nearest neighbor" to each of the 348 central lenses (i.e., those neighboring galaxies with $\theta = \theta_1$). Figures 3, 4, and 5 show the same distributions as Figure 2, but for the second, third, and fourth nearest neighbors, respectively. From Figures 2 through 5, it is clear that the distributions of halo velocity dispersions and redshifts for the neighboring galaxies are nearly identical to those of the central lenses. It is also clear from Figures 2 through 5 that the distribution of redshift differences between the central lenses and their near neighbors is similar in all cases. Note that $\gtrsim 90\%$ of the near neighbor galaxies have $|\delta z| > 0.005$ and are therefore unlikely to be physically associated with the central lenses.

To compute the mean tangential shear around each of the central lenses, a fixed source redshift of $z_s = 1.5$ was adopted. Again, the primary focus of this investigation is the net effect of near neighbors on the galaxy-galaxy lensing signal, so the adoption of a fixed source redshift is sufficient. The sources were assigned intrinsically round shapes and their final shapes were computed as

$$\vec{\chi}_f = \sum_{i=1}^{N_{\rm lens}} \vec{\gamma}_i = \epsilon e^{2i\phi} \tag{7}$$

where $\vec{\gamma}_i$ is the shear due foreground lens i, ϵ is the final, lensed image shape, and ϕ is the orientation of the final, lensed image. Since all of the simulations were performed in the weak lensing regime, Equation 7 yields the net shear experienced by each source. Simulations were performed separately using only the single nearest neighbor, the two nearest neighbors, the three nearest neighbors, and the four nearest neighbors. Therefore, the value of $N_{\rm lens}$ in Equation (7) ranges from 2 to 5. To compute the galaxy-galaxy lensing signal at a given physical separation, r_p, from a central lens galaxy, a ring of 10^6 sources, uniformly distributed in polar angle, was placed around the central lens galaxy at a radius of r_p and the final image shapes of all sources were computed using Equation (7) above. The mean

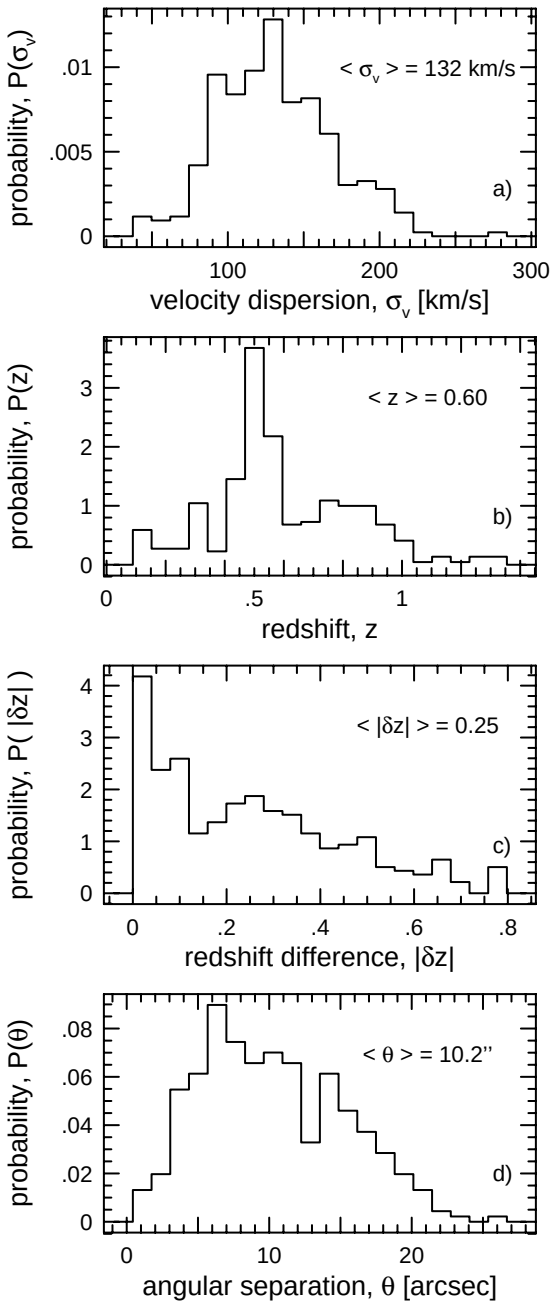

Figure 2. Probability distributions for the nearest neighbors of the central lens galaxies. Panels show: a) velocity dispersion, b) redshift, c) absolute value of the redshift difference between the central lens and neighbor, and d) angular separation between the central lens and neighbor. Mean values for each of the distributions are indicated in the panels. Note that $|\delta z| < 0.005$ for only $\sim 10\%$ of the nearest neighbors.

tangential shear, centered on the central lens, was then computed in the standard way (see, e.g., Schneider 2006) using the final image shapes of the lensed sources.

In addition to the mean tangential shear, the excess surface mass density, $\Delta\Sigma(r_p)$, was computed by numerically sampling the mass density field. To compute the value of $\Sigma(r_p)$ at the location of a given central lens galaxy, a ring of 10^6 sampling points, uniformly distributed in polar angle, was placed at a radius r_p from the central lens. Using Equation (3) above, the total surface mass density due to all lenses was computed at each point on the ring, then the mean value was computed from all 10^6 sampling points. To compute the value of $\langle\Sigma(< r_p)\rangle$ at the location of a central lens galaxy, 10^6 sampling points were uniformly distributed within a circle of radius r_p, centered on the central lens. Again using Equation (3), the total surface mass density due to all lenses was computed at each point within the

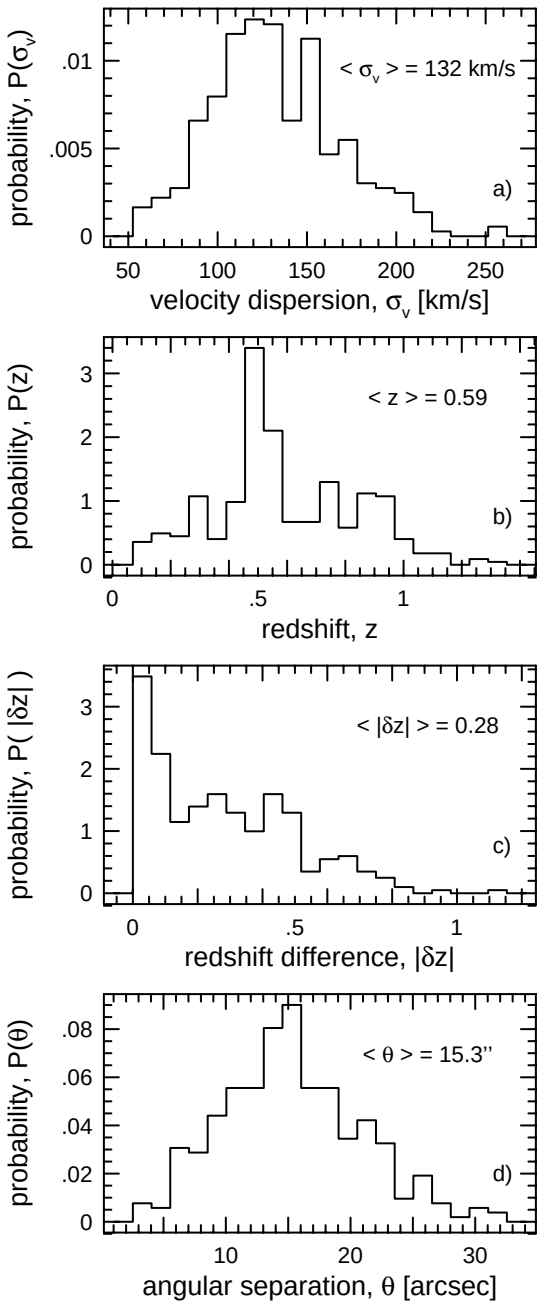

Figure 3. Same as Figure 2, but for the second nearest neighbors. Note that $|\delta z| < 0.005$ for only $\sim 6\%$ of the second nearest neighbors.

circle and the mean value was computed from all 10^6 sampling points. The value of $\Delta\Sigma(r_p)$ was then computed as the difference between $\langle\Sigma(< r_p)\rangle$ obtained from the circle of 10^6 sampling points and the value of $\Sigma(r_p)$ obtained from the ring of 10^6 sampling points. The sampling procedure was repeated 100 times at the location of each central lens galaxy and the final value of $\Delta\Sigma(r_p)$ was taken to be the mean of the results from the 100 independent samplings.

3. RESULTS

Although the spectroscopic redshifts of the lens galaxies are known, the first set of simulations that was performed adopted a fixed lens redshift value of $z_l = 0.6$ (i.e., the mean redshift for the lens galaxies). The reason for this is to demonstrate directly that, as expected, when neighboring lens galaxies are located near to each other in redshift space (i.e., they are physically related), the relationship between the mean tangential shear and the excess surface

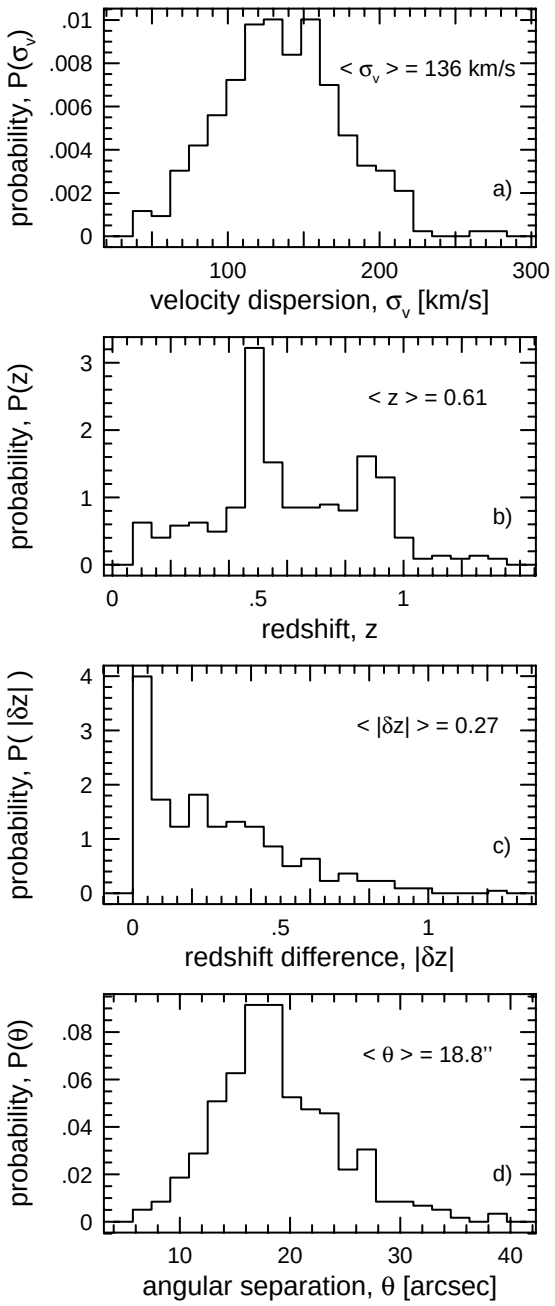

Figure 4. Same as Figure 2, but for the third nearest neighbors. Note that $|\delta z| < 0.005$ for only $\sim 6\%$ of the third nearest neighbors.

mass density, given by

$$\gamma_T(r_p) = \Delta\Sigma(r_p) \times \Sigma_c^{-1}, \tag{8}$$

is indeed valid. Shown in Figure 6 is the mean tangential shear, $\gamma_T(r_p)$, computed around the 348 central lens galaxies with fixed redshift $z_l = 0.6$ (open points). Also shown in Figure 6 is the mean value of the excess surface mass density, $\Delta\Sigma(r_p)$, scaled by the value of the critical surface mass density for a lens with $z_l = 0.6$ and a source with $z_s = 1.5$ (solid points). Error bars for the mean values of $\gamma_T(r_p)$ and $\Delta\Sigma(r_p) \times \Sigma_c^{-1}$ were computed using jackknife resampling and in all cases the error bars are significantly smaller than the sizes of the data points in Figure 6. Figure 6 shows that on small scales, the effects of the near neighbor galaxies on the galaxy-galaxy lensing is negligible. On large scales, however, the effects of weak lensing by the near neighbors are significant and, importantly, the contributions of the near neighbors to the galaxy-galaxy lensing signal do not cancel one another. Shown in Figure 7 is the ratio of the

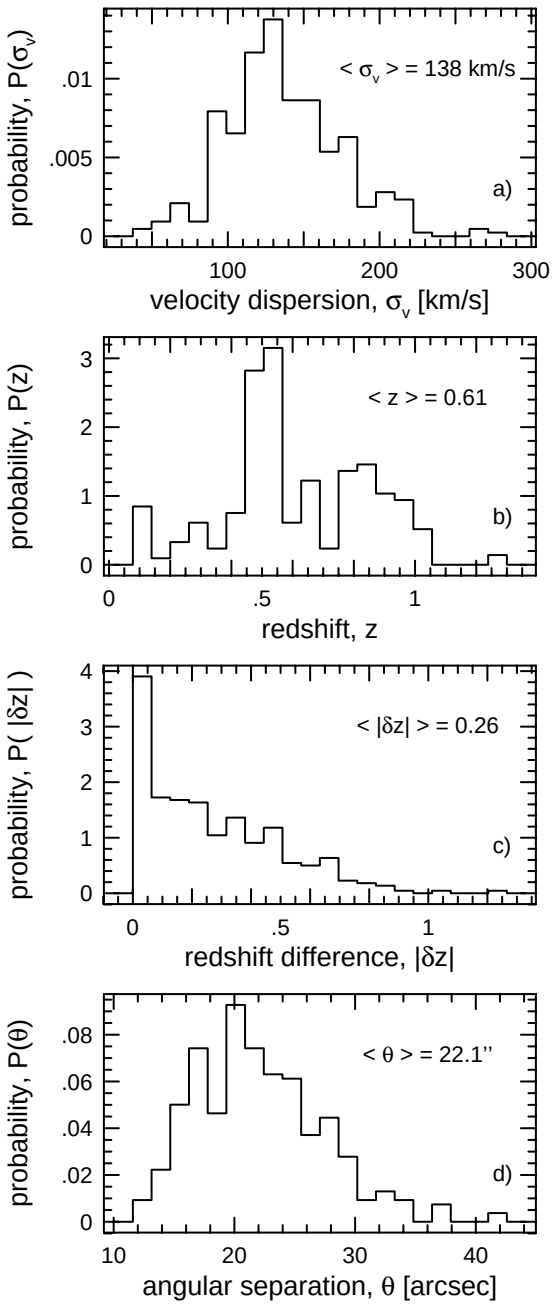

Figure 5. Same as Figure 2, but for the fourth nearest neighbors. Note that $|\delta z| < 0.005$ for only $\sim 6\%$ of the fourth nearest neighbors.

mean tangential shear to the scaled excess surface mass density. From Figure 7, then, the ratio of the mean tangential shear to the scaled excess surface mass density is consistent with unity on all scales. The error bars in Figure 7 were computed by combining the jackknife errors from Figure 6 in quadrature.

Having demonstrated the validity of Equation (8) for the special limit in which the central lens and its near neighbors have identical redshifts, a second set of simulations was run and in this second set of simulations the galaxies were assigned their observed spectroscopic redshifts. Here, when the value of Σ_c is taken to be the critical surface mass density of the central lens, the validity of Equation (8) is no longer assured since the near neighbor galaxies are typically located at redshifts that are significantly different from that of the central lens (see panel c in Figures 2 through 5). Shown in Figure 8 are two different extreme examples of the failure of Equation (8) when a central lens galaxy and its nearest neighbor are located at significantly different redshifts. In Figure 8 the calculations were performed using

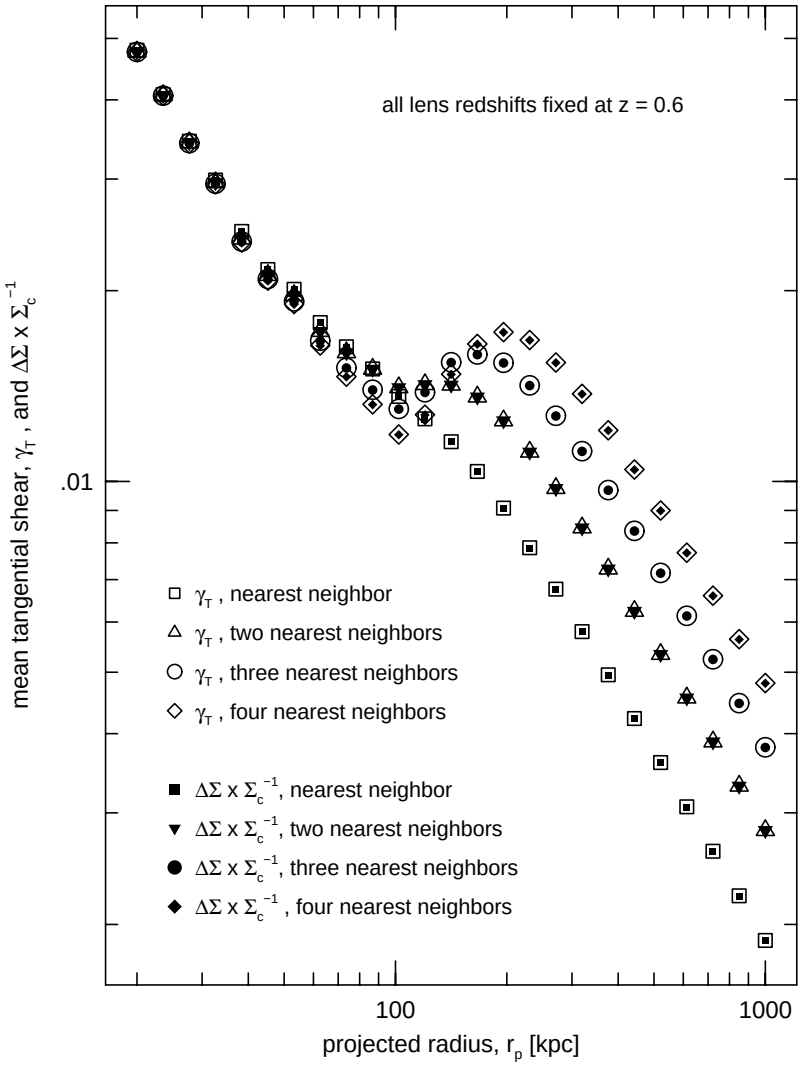
all lens redshifts fixed at z = 0.6
mean tangential shear, γ_T , and $\Delta\Sigma \times \Sigma_c^{-1}$
.01
100
1000
projected radius, r_p [kpc]
γ_T , nearest neighbor
γ_T , two nearest neighbors
γ_T , three nearest neighbors
γ_T , four nearest neighbors
$\Delta\Sigma \times \Sigma_c^{-1}$, nearest neighbor
$\Delta\Sigma \times \Sigma_c^{-1}$, two nearest neighbors
$\Delta\Sigma \times \Sigma_c^{-1}$, three nearest neighbors
$\Delta\Sigma \times \Sigma_c^{-1}$, four nearest neighbors

Figure 6. Mean tangential shear, $\gamma_T(r_p)$, and scaled excess surface mass density, $\Delta\Sigma(r_p) \times \Sigma_c^{-1}$, computed using all 348 central lens galaxies, but with the redshifts of the lenses fixed at $z_l = 0.6$. Squares: central lens and its nearest neighbor only. Triangles: central lens and its two nearest neighbors. Circles: central lens and its three nearest neighbors. Diamonds: central lens and its four nearest neighbors. Open points: $\gamma_T(r_p)$. Filled points: $\Delta\Sigma(r_p) \times \Sigma_c^{-1}$.

the central lens galaxy and its single nearest neighbor. In both cases, the halo of the central lens galaxy in Figure 8 has a velocity dispersion that is comparable to the mean value for all 348 central lenses. In the top panel of Figure 8, $\gamma_T(r_p)$ agrees with $\Delta\Sigma(r_p) \times \Sigma_c^{-1}$ on small scales; however, on large scales $\Delta\Sigma(r_p) \times \Sigma_c^{-1}$ exceeds $\gamma_T(r_p)$ by $\sim 30\%$. (Note that the steep "dip" in the curves shown in the top panel of Figure 8 occurs at a scale comparable to the spacing between the two lenses and such features are commonly seen in theoretical weak lensing profiles when more than one lens is present.) In the bottom panel of Figure 8, $\gamma_T(r_p)$ exceeds $\Delta\Sigma(r_p) \times \Sigma_c^{-1}$ by $\sim 30\%$ over all but the smallest scales that are shown. The velocity dispersions of the two lenses in the top panel are 132 km sec^{-1} (central lens) and 214 km sec^{-1} (nearest neighbor). The redshifts of the two lenses in the top panel are 0.85 (central lens) and 1.13 (nearest neighbor), and the separation between the lenses is $\theta_1 = 8.9$" (corresponding to a projected separation of $r_p \sim 70$ kpc at the redshift of the central lens). The velocity dispersions of the two lenses in the bottom panel are 134 km sec^{-1} (central lens) and 128 km sec^{-1} (nearest neighbor). The redshifts of the two lenses in the bottom panel are 0.93 (central lens) and 0.52 (nearest neighbor), and the separation between the lenses is $\theta_1 = 2.2$" (corresponding to a projected separation of $r_p \sim 18$ kpc at the redshift of the central lens).

Although the differences between $\gamma_T(r_p)$ and $\Delta\Sigma(r_p) \times \Sigma_c^{-1}$ are substantial for the two central lenses shown in Figure 8, the sense of the discrepancy (i.e., greater or less than unity) is opposite. Therefore, it is to be expected that, when computed over the entire population of central lens galaxies, some of the discrepancy between $\gamma_T(\theta)$ and

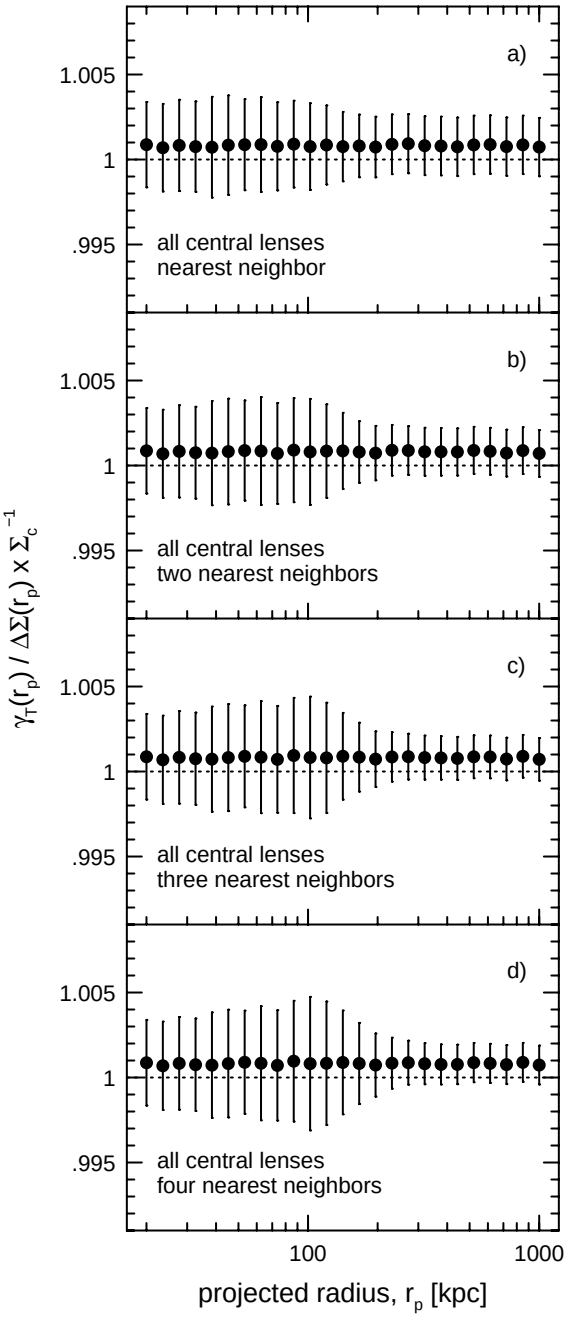

Figure 7. Ratios of the curves shown in Figure 6, $\gamma_T(r_p) \div \Delta\Sigma(r_p) \times \Sigma_c^{-1}$. Panels show ratios for different numbers of near neighbors in the calculations: a) central lens and its nearest neighbor only, b) central lens and its two nearest neighbors, c) central lens and its three nearest neighbors, and d) central lens and its four nearest neighbors. As expected, the ratio is consistent with unity on all scales.

$\Delta\Sigma(r_p) \times \Sigma_c^{-1}$ that is seen for individual lenses will necessarily be averaged away. Results for the mean tangential shear, averaged over all 348 central lenses, are shown by the open points in Figure 9. Solid points in Figure 9 show the mean value of $\Delta\Sigma(r_p) \times \Sigma_c^{-1}$, where Σ_c is the value of the critical surface mass density that is appropriate for the central lens, given its actual redshift. This is analogous to observational studies of galaxy-galaxy lensing in which the observed mean tangential shear is converted into a value of the excess surface mass density by multiplying by the critical surface mass density for the central lens. Here jackknife error bars were again computed and all of the resulting error bars are smaller than the individual data points in Figure 9. As with the case when all lens galaxies were placed at a fixed redshift of $z_l = 0.6$ (Figure 6 above), the effect of the near neighbor galaxies on the mean tangential shear is small on small scales, but is significant on large scales. Again, as in Figure 6, the effects of the near neighbor galaxies

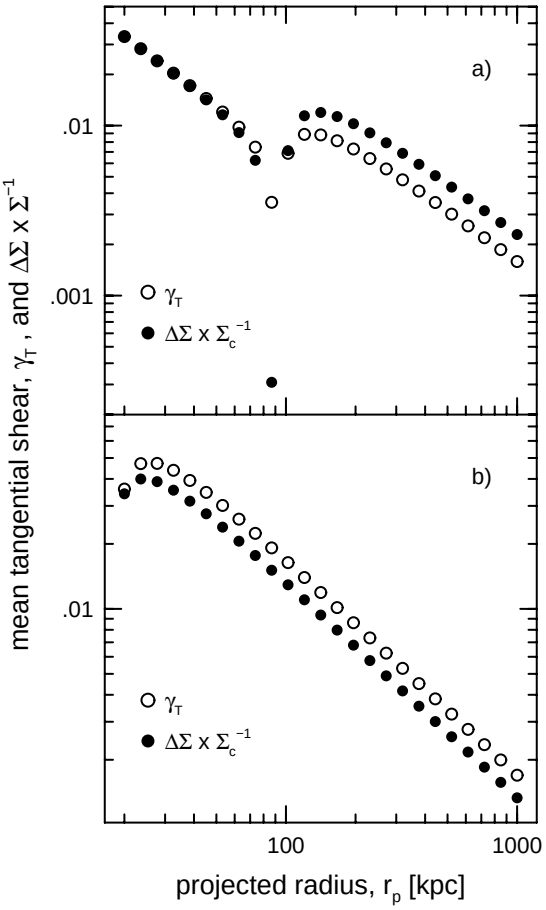

Figure 8. Two extreme examples of the failure of Equation (8) when the central lens galaxy and the nearest neighbor lens galaxy have different redshifts. *Top:* Central lens has velocity dispersion $\sigma_v = 132$ km sec^{-1} and redshift $z_l = 0.85$. Nearest neighbor lens has velocity dispersion $\sigma_v = 214$ km sec^{-1} and redshift $z_l = 1.13$. Separation between the two lenses on the sky corresponds to $r_p \sim 70$ kpc at the redshift of the central lens. *Bottom:* Central lens has velocity dispersion $\sigma_v = 134$ km sec^{-1} and redshift $z_l = 0.93$. Nearest neighbor lens has velocity dispersion $\sigma_v = 128$ km sec^{-1} and redshift $z_l = 0.52$. Separation between the two lenses on the sky corresponds to $r_p \sim 18$ kpc at the redshift of the central lens. Circles: mean tangential shear, $\gamma_T(r_p)$. Squares: scaled excess surface mass density, $\Delta\Sigma(r_p) \times \Sigma_c^{-1}$, where Σ_c is the value of the critical surface mass density for the central lens.

on the mean tangential shear do not cancel each other on large scales. Also, unlike the case when all lens galaxies were placed a single, fixed redshift, a difference between the values of $\gamma_T(r_p)$ and $\Delta\Sigma(r_p) \times \Sigma_c^{-1}$ manifests when the redshifts of the lens galaxies are taken to be their actual, observed spectroscopic redshifts. That is, Equation (8) is no longer strictly valid due to the fact that the value of Σ_c necessarily differs for the central lenses and their near neighbors.

Shown in Figure 10 is the ratio of the mean tangential shear to the scaled excess surface mass density for the curves shown in Figure 9. As with Figure 7, the error bars in Figure 10 were obtained by combining the error bars from Figure 9 in quadrature. From Figure 10, it is clear that, over the majority of scales for which the weak lensing signal was computed, the value of $\Delta\Sigma(r_p) \times \Sigma_c^{-1}$ exceeds the value of $\gamma_T(r_p)$. The ratio of $\gamma_T(r_p)$ to $\Delta\Sigma(r_p) \times \Sigma_c^{-1}$ is not monotonic and ranges from unity on the smallest scales ($r_p \lesssim 20$ kpc) to greater than unity on larger, but "galactic", scales (30 kpc $\lesssim r_p \lesssim$ 60 kpc) to less than unity on the largest scales ($r_p \gtrsim 100$ kpc). From Figures 9 and 10, it is also clear that adding an increasing number of near neighbors into the calculation of the net weak lensing signal increases the value of the mean tangential shear at large lens-source separations. Adding an increasing number near neighbors also increases the degree to which $\gamma_T(r_p)$ and $\Delta\Sigma(r_p) \times \Sigma_c^{-1}$ disagree with each other on the largest scales (i.e., ranging from a difference of $\sim 1\%$ for the case of one central lens and its single nearest neighbor to a difference of $\sim 2\%$ for the case of one central lens and its four nearest neighbors).

The results shown in Figures 9 and 10 are those that are obtained when $\gamma_T(r_p)$ and $\Delta\Sigma(r_p) \times \Sigma_c^{-1}$ are averaged over the entire population of 348 central lenses. Given the wide range of velocity dispersions for the halos of the lens

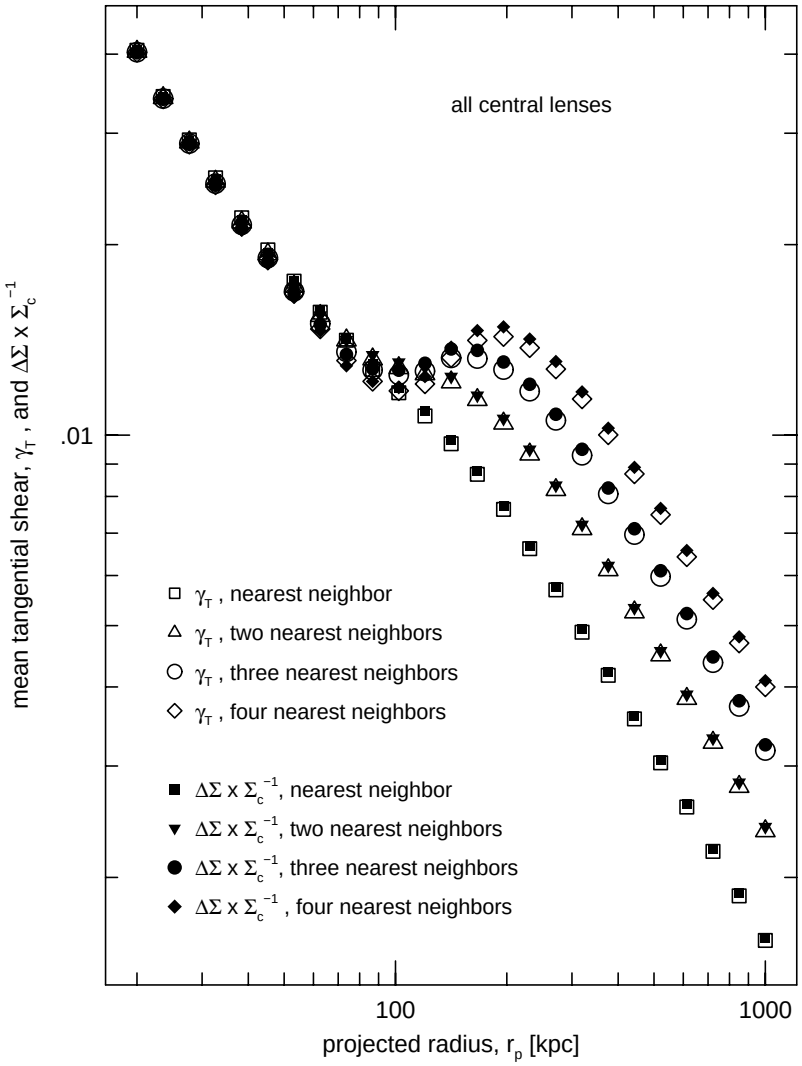
all central lenses
mean tangential shear, γ_T, and $\Delta\Sigma \times \Sigma_c^{-1}$
.01
γ_T, nearest neighbor
γ_T, two nearest neighbors
γ_T, three nearest neighbors
γ_T, four nearest neighbors
$\Delta\Sigma \times \Sigma_c^{-1}$, nearest neighbor
$\Delta\Sigma \times \Sigma_c^{-1}$, two nearest neighbors
$\Delta\Sigma \times \Sigma_c^{-1}$, three nearest neighbors
$\Delta\Sigma \times \Sigma_c^{-1}$, four nearest neighbors
100
1000
projected radius, r_p [kpc]

Figure 9. Mean tangential shear, $\gamma_T(r_p)$, and scaled excess surface mass density, $\Delta\Sigma(r_p) \times \Sigma_c^{-1}$, computed using all 348 central lens galaxies. Unlike Figure 6, here the redshifts of the lenses are taken to be their observed spectroscopic redshifts. Squares: central lens and its nearest neighbor only. Triangles: central lens and its two nearest neighbors. Circles: central lens and its three nearest neighbors. Diamonds: central lens and its four nearest neighbors. Open points: $\gamma_T(r_p)$. Filled points: $\Delta\Sigma(r_p) \times \Sigma_c^{-1}$.

galaxies, however, it is entirely possible that the net effects of the near neighbors on the weak lensing signal could vary with the velocity dispersions of the central lenses. To investigate this, $\gamma_T(r_p)$ and $\Delta\Sigma(r_p) \times \Sigma_c^{-1}$ were separately computed using central lenses with higher than average halo velocity dispersions ($\sigma_v > 133$ km sec^{-1}, 166 galaxies) and lower than average halo velocity dispersions ($\sigma_v < 133$ km sec^{-1}, 182 galaxies). Results for central lenses with higher than average velocity dispersions are shown in Figures 11 and 13. Results for central lenses with lower than average velocity dispersions are shown in Figures 12 and 14. Over the entire range of scales for which the signal was computed, the ratio of $\gamma_T(r_p)$ to $\Delta\Sigma(r_p) \times \Sigma_c^{-1}$ for the high-velocity dispersion central lenses tracks in the opposite direction than it does for the low-velocity dispersion central lenses. That is, when the ratio is greater than unity for the high-velocity dispersion central lenses, it is less than unity for the low-velocity dispersion central lenses, and when the ratio is less than unity for the high-velocity dispersion central lenses it is greater than unity for the low-velocity dispersion central lenses. Because of this, the differences between $\gamma_T(r_p)$ and $\Delta\Sigma(r_p) \times \Sigma_c^{-1}$ when averaged over the entire population of lenses are significantly less than when they are averaged over the subsets of high- and low-velocity dispersion central lenses.

From Figures 11, 12, 13, and 14, it is clear that physically unrelated near neighbors affect the weak lensing signal for both high- and low-velocity dispersion central lenses, but to differing degrees. In the case of high-velocity dispersion

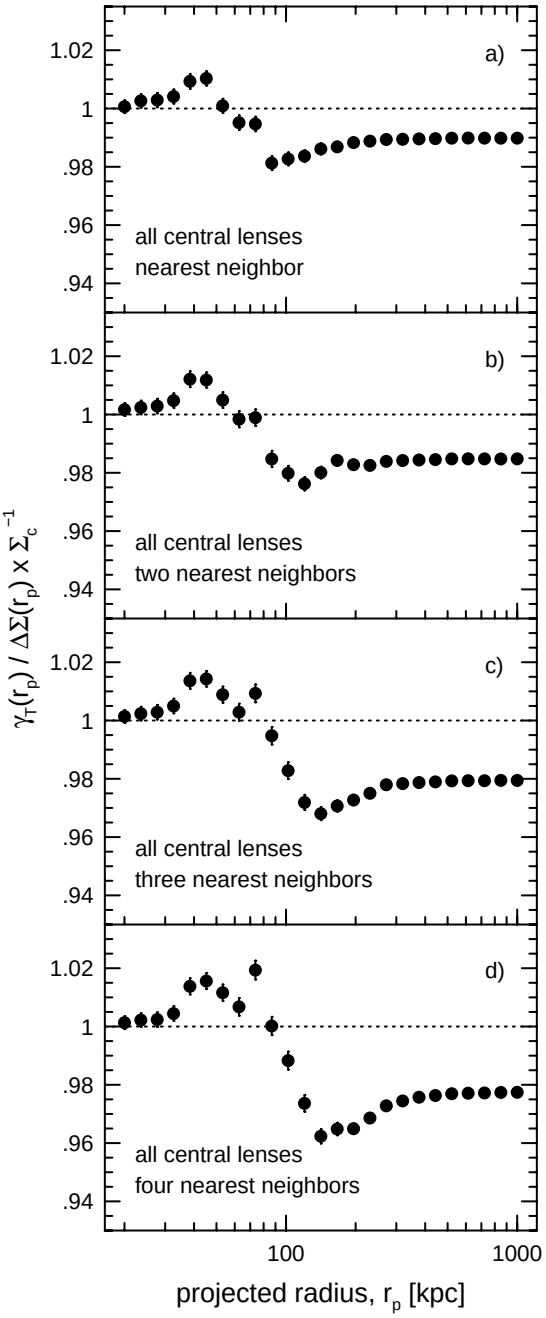

Figure 10. Ratios of the curves shown in Figure 9, $\gamma_T(r_p) \div \Delta\Sigma(r_p) \times \Sigma_c^{-1}$. Panels show ratios for different numbers of near neighbors: a) central lens and its nearest neighbor only, b) central lens and its two nearest neighbors, c) central lens and its three nearest neighbors, and d) central lens and its four nearest neighbors. Unlike Figure 7, here the redshifts of the lenses are taken to be their observed spectroscopic redshifts. The broad redshift distribution of the lens galaxies causes the ratio of the mean tangential shear to the scaled excess surface mass density to deviate from unity over most scales.

central lenses (Figures 11 and 13), the value of $\gamma_T(r_p)$ on large scales exceeds that of $\Delta\Sigma(r_p) \times \Sigma_c^{-1}$, and the difference between the two quantities ranges from $\sim 1.5\%$ for the case of one central lens and its single nearest neighbor to $\sim 2.5\%$ for the case of one central lens and its four nearest neighbors. In the case of low-velocity dispersion central lenses (Figures 12 and 14), the weak lensing signal is much more strongly affected by physically unrelated near neighbors than is the weak lensing signal for high-velocity dispersion central lenses. On the largest scales, the differences between $\gamma_T(r_p)$ and $\Delta\Sigma(r_p) \times \Sigma_c^{-1}$ for the low-velocity dispersion central lenses range from $\sim 4.5\%$ (for the case of a central lens and its single nearest neighbor) to $\sim 7\%$ (for the case of a central lens and its four nearest neighbors).

Lastly, shown in Figure 15 is the probability distribution for the ratio of the mean tangential shear to the scaled

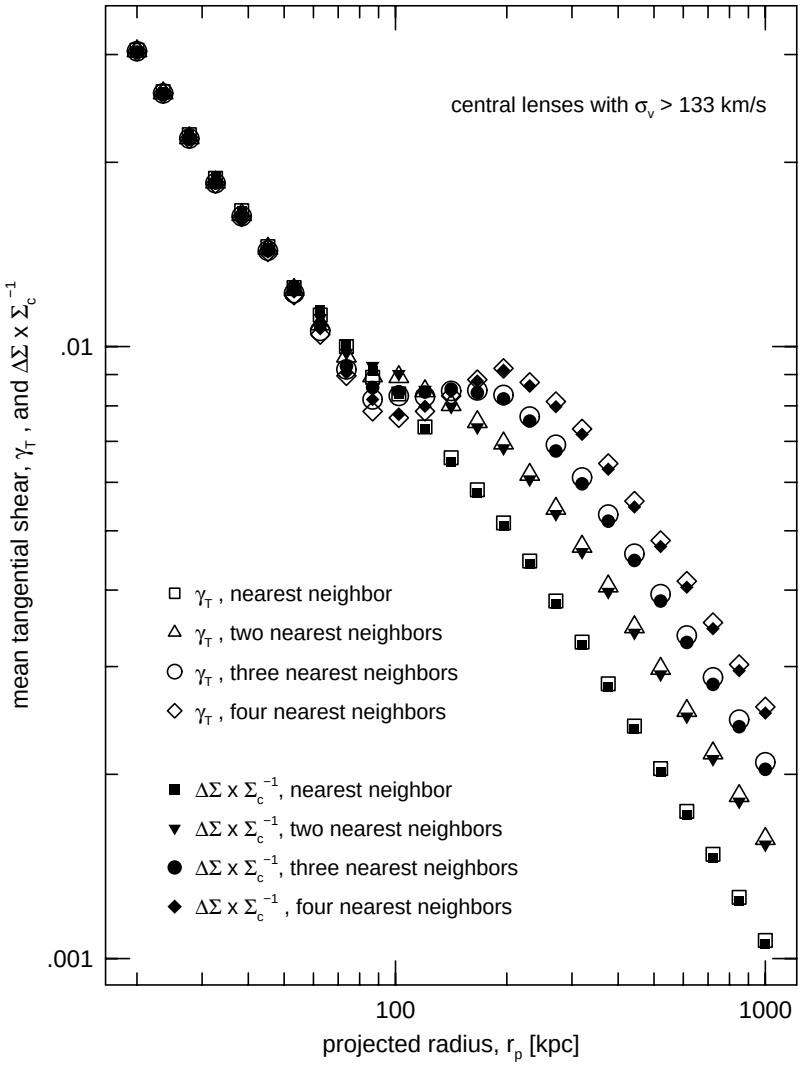
central lenses with σv > 133 km/s
mean tangential shear, γT , and ΔΣ x Σc−1
.01
.001
100
1000
projected radius, rp [kpc]
γT , nearest neighbor
γT , two nearest neighbors
γT , three nearest neighbors
γT , four nearest neighbors
ΔΣ x Σc−1, nearest neighbor
ΔΣ x Σc−1, two nearest neighbors
ΔΣ x Σc−1, three nearest neighbors
ΔΣ x Σc−1 , four nearest neighbors

Figure 11. Same as Figure 9, but for the 166 central lenses with higher than average velocity dispersions.

excess surface mass density, evaluated at $r_p = 1$ Mpc. The left panels in Figure 15 show the results averaged over all 348 central lens galaxies, while the center and right panels show the results for the low-velocity dispersion central lenses and the high-velocity dispersion central lenses, respectively. From top to bottom, the panels in Figure 15 show the results for calculations that include only the nearest neighbor (topmost panels), the two nearest neighbors, the three nearest neighbors, and the four nearest neighbors (bottommost panels). The dotted vertical lines indicate a value of unity. From Figure 15, then, in all cases the ratio of the mean tangential shear to the scaled excess surface mass density at large scales has a probability distribution that is both broad and asymmetrical. For a given central lens, the ratio of the mean tangential shear to the scaled excess surface mass density at $r_p = 1$ Mpc spans a range from ~ 0.5 to ~ 1.5, and the shape of the probability distribution is a strong function of the velocity dispersions of the central lenses. That is, for a given low-velocity dispersion central lens, the asymmetry of the probability distribution is such that the scaled excess surface mass density typically exceeds the mean tangential shear. For a given high-velocity dispersion central lens, the asymmetry of the probability distribution is such that the mean tangential shear tends to exceed the scaled excess surface mass density.

4. SUMMARY AND DISCUSSION

The observed celestial coordinates, spectroscopic redshifts, and rest-frame blue luminosities of galaxies in the region of the HDF-N were used as the basis of a suite of Monte Carlo simulations of weak galaxy-galaxy lensing. Since the simulations incorporate known galaxies with a uniform completeness in redshift space ($R \leq 23$), the simulations

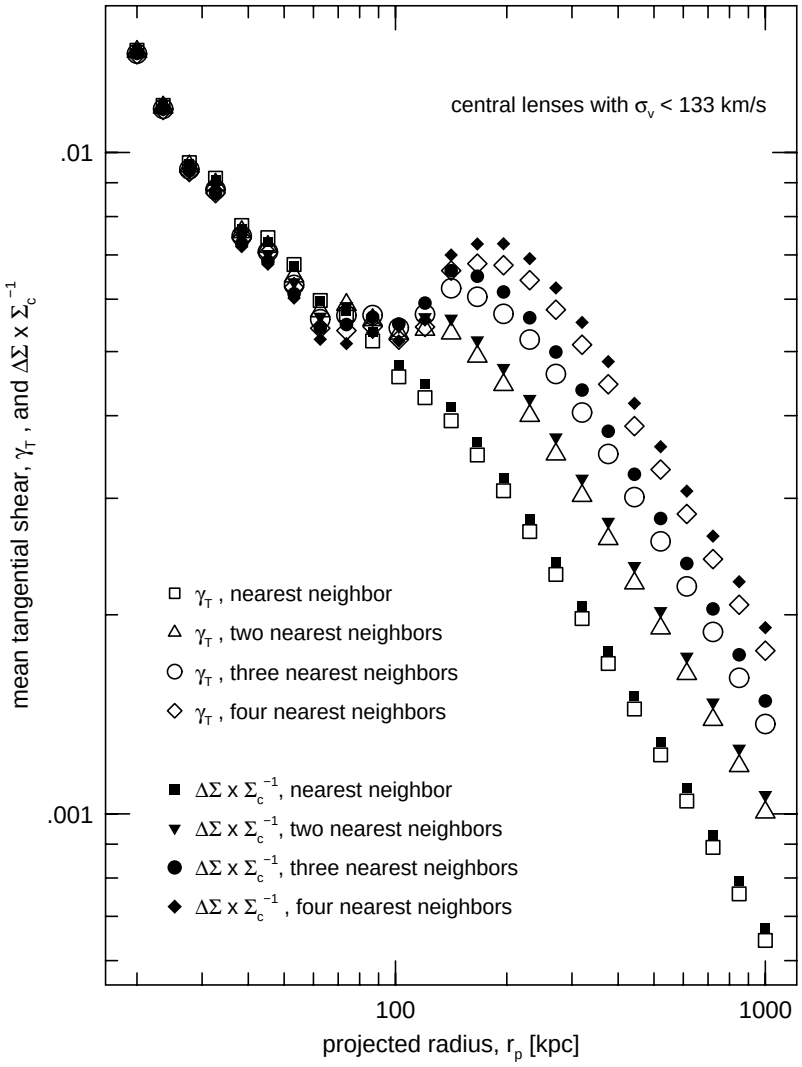
central lenses with σv < 133 km/s
.01
.001
mean tangential shear, γT , and ΔΣ x Σc-1
γT , nearest neighbor
γT , two nearest neighbors
γT , three nearest neighbors
γT , four nearest neighbors
ΔΣ x Σc-1, nearest neighbor
ΔΣ x Σc-1, two nearest neighbors
ΔΣ x Σc-1, three nearest neighbors
ΔΣ x Σc-1 , four nearest neighbors
100
1000
projected radius, rp [kpc]

Figure 12. Same as Figure 9, but for the 182 central lenses with lower than average velocity dispersions.

naturally incorporate the intrinsic redshift distribution, mass distribution, and clustering of galaxies in our Universe. The simulations investigated the effects of near-neighbor galaxies on the mean tangential shear, computed around central lens galaxies, and the relationship between the mean tangential shear and the excess surface mass density, scaled by the critical surface mass density of the central lens. The main results from the simulations are as follows:

1. As expected, the relationship between the mean tangential shear and the scaled excess surface mass density is given by $\gamma(r_p) = \Delta\Sigma(r_p) \times \Sigma_c^{-1}$ when all lens galaxies are assigned a fixed, identical redshift.

2. When the lens galaxies are assigned their observed spectroscopic redshifts, the value of $\gamma(r_p)$ may differ from that of $\Delta\Sigma(r_p) \times \Sigma_c^{-1}$. This is due to the fact that the majority of the near neighbors have redshifts that are significantly different from those of the central lenses.

3. At large scales, the ratio of the mean tangential shear to the scaled excess surface mass density for a given central lens galaxy spans a wide range, from ~ 0.5 to ~ 1.5.

4. The magnitude and sense (i.e., greater or less than unity) of the discrepancy between the mean tangential shear and the scaled excess surface mass density are functions of both the physical scale, r_p, and the velocity dispersions of the central lenses. In particular, at large scales the difference between the mean tangential shear and the scaled excess surface mass density is considerably greater for low-velocity dispersion central lenses than it is for high-velocity dispersion central lenses.

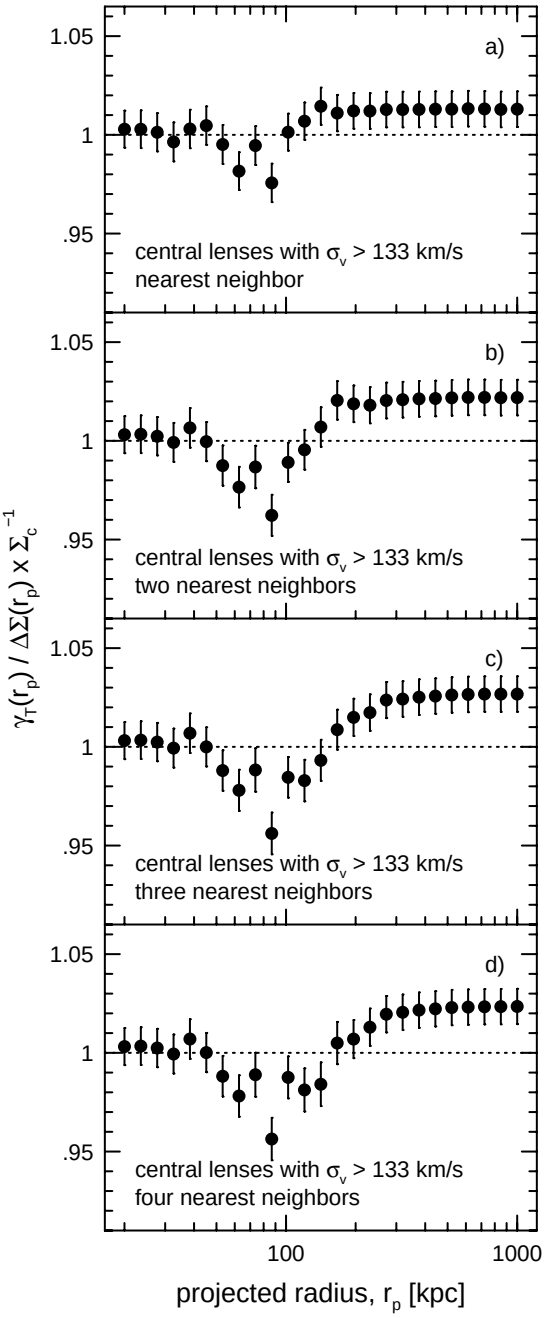

Figure 13. Same as Figure 10, but for the 166 central lenses with higher than average velocity dispersions.

5. The effects of physically unrelated near-neighbors on the weak lensing shear signal do not cancel out. Instead, physically unrelated near-neighbors increase the mean tangential shear on scales larger than the separation between the central lens and its neighbors.

The significance of this work is a demonstration that, in the limit of a realistic redshift distribution for weak galaxy lenses, systematic errors should arise when the common method of converting an observed galaxy-galaxy lensing signal into a constraint on the excess surface mass density is used (i.e., multiplication of the value of γ_T for a given source galaxy by the value of Σ_c for the central lens and that particular source galaxy). This is because neighboring lens galaxies that are located at redshifts other than the redshift of the central lens give rise to a substantial component of the net weak lensing shear. An important goal for future, deep weak lensing surveys (for example, those that will be yielded by the Large Synoptic Survey Telescope, *Euclid*, and *WFIRST*) is a constraint on the mass distribution

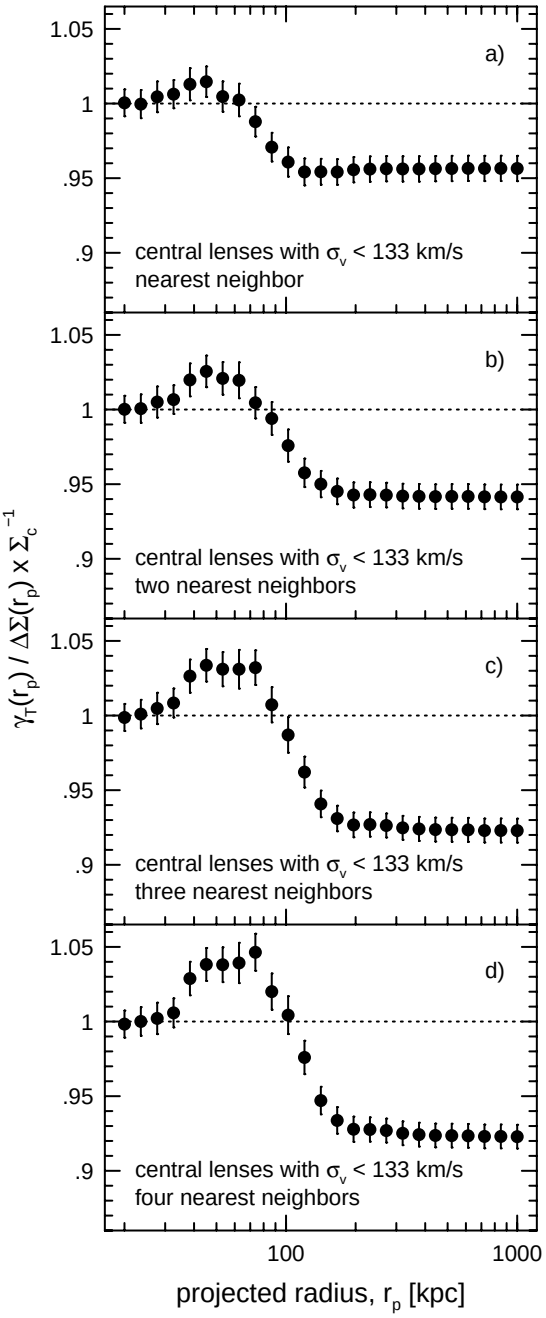

Figure 14. Same as Figure 10, but for the 182 central lenses with lower than average velocity dispersions.

of the universe that is accurate to $\lesssim 1\%$ on scales $r_p > 1$ Mpc. The results of this work suggest, therefore, that in order to achieve such an accurate measurement of the mass density from future galaxy-galaxy lensing studies, it may be important to move beyond the methods that are currently used to convert the observed galaxy-galaxy lensing signal into a measurement of the excess surface mass density. This is due to the fact that, to date, most theoretical predictions for the galaxy-galaxy lensing signal have adopted a model in which the two-halo term (i.e., the contribution to the weak lensing signal caused by galaxies other than the central lens) is attributed to neighboring galaxies that are physically related to the central galaxy (i.e., the neighboring lens galaxies that contribute to the net shear are assumed to be located at the same redshift as the central galaxy). Noteable exceptions to this include Schrabback et al. (2015) and Saghiha et al. (2016), both of which utilized direct ray-traying through N-body simulations to predict the galaxy-galaxy lensing signal using the methods described by Hilbert et al. (2009).

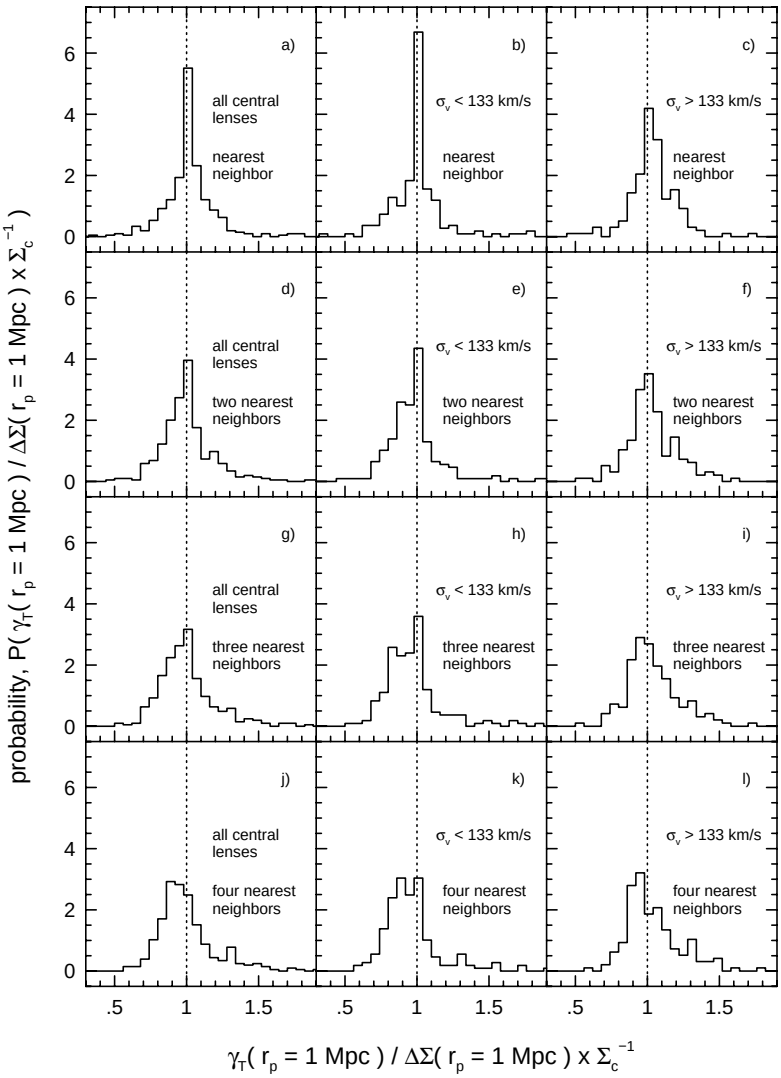

Figure 15. Probability distributions for the ratio of the mean tangential shear to the scaled excess surface mass density, evaluated at a projected radial distance of $r_p = 1$ Mpc from the central lenses. Vertical dotted lines indicate a value of unity. *Left:* Results from all 348 central lenses. *Center:* Results from the 182 central lenses with lower than average velocity dispersions. *Right:* Results from the 168 central lenses with higher than average velocity dispersions. From top to bottom, the panels show the results for the central lens and its nearest neighbor (topmost panels), the central lens and its two nearest neighbors, the central lens and its three nearest neighbors, and the central lens and its four nearest neighbors (bottommost panels). For a given central lens, the ratio takes on a wide range of values (from ~ 0.5 to ~ 1.5) and the probability distribution is highly asymmetrical in all cases. Averaged over the population of central lenses, the asymmetry of the probability distribution leads to a net discrepancy between the mean tangential shear and the scaled surface mass density (see Figures 10, 13, and 14).

The simulations presented here demonstrate that, in a sufficiently deep data set, the majority of near neighbors are not physically related to the central lens, and these physically unrelated near neighbors give rise to a significant component of the net galaxy-galaxy lensing signal on large scales. Based upon the results presented here, the need to explicitly include the effects of physically unrelated near neighbors may be especially important when attempting to constrain the dependence of $\Delta\Sigma(r_p)$ on the physical properties of the central lens galaxies (e.g., luminosity, color, stellar mass). Indeed, although the significance is somewhat low, there may already be an indication in existing galaxy-galaxy lensing observations that physically unassociated near neighbors are contributing to the observed signal. For example, Velander et al. (2014) found that their adopted model for the one- and two-halo terms provided good fits to the galaxy-galaxy lensing signal when the signal was computed using the entire population of central lens galaxies and also when it was computed separately for red central lenses. However, their model did not provide a good overall fit to the galaxy-galaxy lensing signal for blue central lenses with low luminosities and low stellar masses. The work presented here suggests that, if physically unassociated near neighbors are contributing to the galaxy-galaxy lensing

signal, then the largest discrepancies between the model adopted by Velander et al. (2014) and the observed mean tangential shear should, in fact, manifest in the regime of the lowest-luminosity, lowest-mass central galaxies.

The degree to which the observed mean tangential shear will differ from the actual scaled excess surface mass density in any large, future survey will, of course, depend upon the redshift distribution of the foreground lenses and the nature of the dark matter halos that surround them. For the sake of simplicity, here an unphysical isothermal sphere model was adopted for the halos of the lens galaxies. This was done in order to construct a demonstration of the effects of near neighbor galaxies on the galaxy-galaxy lensing signal that is straightforward to reproduce. Because of the simplicity of the adopted halo mass distribution, and because the effects of all possible foreground lens galaxies were not expressly included here (i.e., the simulations were limited to at most the contribution of the four nearest neighbors), the simulations presented here do not represent an accurate estimate of the degree of discrepancy between the mean tangential shear and the scaled excess surface mass density that would be expected to occur in our Universe. Rather, it is generally agreed that the mass density of our Universe is dominated by CDM, for which the dark matter halos of galaxies are not isothermal. The shear profile of a CDM halo differs from that of an isothermal sphere, being shallower than isothermal on scales less than the scale radius of the halo and steeper than isothermal on scales greater than the scale radius of the halo (see, e.g., Figure 1 of Wright & Brainerd 2000). An accurate estimate of the degree of discrepancy between the mean tangential shear and the scaled excess surface mass density that could be expected in our Universe therefore awaits a more thorough analysis, such as could be obtained from high-resolution CDM simulations that include luminous galaxies via either semi-analytic galaxy formation or numerical hydrodynamics.

Animated, insightful conversations with Kelly Blumenthal, Dave Goldberg, and Brandon Harrison, as well as support from the NASA Astrophysics Theory Program via grant NNX13AH24G S04, are gratefully acknowledged.

REFERENCES

Brainerd, T. G. 2010, ApJ, 713, 603
Brainerd, T. G., Blandford, R. D. & Smail, I. 1996, ApJ, ApJ, 466, 623
Brimioulle, F., Seitz, S., Lerchster, M., Bender, R., & Snigula, J. 2013, MNRAS, 432, 1046
Brouwer, M. M. et al. (2016), arXiv:1604.07233
Clampitt, J. et al. (2016), arXiv:1603.05790
Cohen, J. G. 2001, AJ, 121, 2895
Cohen, J. G., Cowie, L. L., Hogg, D. W., Songaila, A., Blandford, R., Hu, E. M. & Shopbell, P. 1996, ApJ, 471, L5
Cohen, J. G., Hogg, D. W., Blandford, R., Cowie, L. L., Hu, E., Songaila, A., Shopbell, P., & Richberg, K. 2000, ApJ, 538, 29
Coupon, J. et al. 2015, MNRAS, 449, 1352
Dell' Antonio, I. P. & Tyson, J. A. 1996, ApJ 473, L17
Driver, S. P. 2009, Astron. Geophys., 50, 050000
Driver, S. P. 2011, MNRAS, 413, 971
Erben, T. 2013, MNRAS, 433, 2545
Fischer, P. et al. AJ, 129, 11981
Flaugher, B. 2005, IJPA, 20, 3121
Gilbank, D. G., Gladders, M. D., Yee, H. K. C. & Hsieh, B. C. 2011, AJ, 141, 94
Griffiths, R. E., Casertano, S., Im, M. & Ratnatunga, K. U. 1996, MNRAS, 282, 1159
Guzik, J. & Seljak, U. 2002, MNRAS, 335, 311
Heymans, C., Bell, E. F., Rix, H.-W., Barden, M., Borch, A., Caldwell, J. A. R., McIntosh, D. H., Meisenheimer, K., Peng, C. Y., Wolf, C., Beckwith, S. V. W., Haussler, B., Jahnke, K., Jogee, S., Sanchez, S. F., Somerville, R. & Wisotzki, L. 2006, MNRAS, 371, L60
Heymans, C. et al. 2012, MNRAS, 427, 146
Hilbert, S., Hartlap, J., White, S. D. M. & Schneider, P. 2009, AA, 499, 31
Hoekstra, H., Yee, H. K. C. & Gladders, M. D. 2004, ApJ, 606, 67
Hoekstra, H., Hsieh, B. C., Yee, H. K. C., Lin, H. & Gladders, M. D. 2005, ApJ, 653, 73
Hogg, D. W., Pahre, M. A., Adelberger, K. L., Blandford, R., Cohen, J. G., Gautier, T. N., Jarrett, T., Neugebauer, G. & Steidel, C. C. 2000, ApJS, 127, 1
Hudson, M. J., Gwyn, S. D. J., Dahle, H. & Kaiser, N. 1998, ApJ, 503, 531
Hudson, M. J. et al. 2015, MNRAS, 447, 298
Kleinheinrich, M., Schneider, P., Rix, H.-W., Erben, T., Wolf, C., Schirmer, M., Meisenheimer, K., Borch, A., Dye, S., Kovacs, Z. & Wisotzki, L. 2006, AA, 455, 441
Kuijken, K. et al. 2015, MNRAS, 454, 3500
Koekemoer, A. M. et al. 2007, ApJS, 172, 196
Leauthaud et al. 2012a, ApJ, 744, 159
Leauthaud et al. 2012b, ApJ, 746, 95
Liske, J. et al. 2015, MNRAS, 452, 2087
Lowenthal, J. D., et al. 1997 ApJ, 481, 673
Mandelbaum, R. 2015 in "Galaxy Masses as Constraints of Formation Models", Proceedings of IAU Symposium 311, M. Cappellari & S. Courteau (eds.)
Mandelbaum, R., Hirata, C., Seljak, U., Guzik, J, Padmanabhan, N., Blake, C., Blanton, M. R., Lupton, R. & Brinkmann, J. 2005, MNRAS, 361, 1287
Mandelbaum, R., Seljak, U., Kauffmann, G., Hirata, C. M. & Brinkmann, J. 2006, MNRAS, 368, 715
Mandelbaum, R., Wang, W., Zu, Y., White, S., Henriques, B. & More, S. 2016, MNRAS, 457, 3200
Miralda-Escudé, J. 1991, ApJ, 370, 1
Phillips, A. C., Guzman, R., Gallego, J., Koo, D. C., Lowenthal, J. D., Vogt, N. P., Faber, S. M. & Illingworth, G. D. 1997, ApJ, 489, 543
Saghiha, H., Simon, P., Schneider, P. & Hilbert, S. 2016, arXiv:1608.08629
Schneider, P. 2006 in "Gravitational Lensing: Strong, Weak and Micro", Saas-Fee Advanced Course 33, Meylan, G., Jetzer, P., & North, P. (eds.), (Berlin:Springer)
Schrabback, T. et al. 2015, MNRAS, 454, 1432
Scoville, N. et al 2007a, ApJS, 172, 1

Scoville, N. et al 2007b, ApJS, 172, 38
Sheldon, E., Johnston, D. E., Frieman, J. A., Scranton, R., McKay, T. A., Connolly, A. J., Budavari, T., Zehavi, I., Bahcall, N. A., Brinkmann, J. & Fukugita, M. 2004, AJ, 127, 2544
Steidel, C. C., Giavalisco, M., Dickinson, M. & Adelberger, K. L. 1996, AJ, 112, 352
Tian, L., Hoekstra, H. & Zhao, H. 2009, MNRAS, 393, 885
Tinker, J. L., Leauthaud, A., Bundy, K., George, M. R., Behroozi, P., Massey, R., Rhodes, J. Wechsler, R. H. 2013, ApJ, 778, 93
van Uitert, E., Hoekstra, H., Velander, M., Gilbank, D. G., Gladders, M. D. & Yee, H. K. C. 2011, AA, 534, A14
van Uitert, E., Cacciato, M., Hoekstra, H. & Herbonnet, R. 2015, AA, 579, A26
van Uitert, E. et al. 2016, MNRAS, 459, 3251
Velander, M. et al. 2014, MNRAS, 437, 2111
Williams, R. E. et al. 1996, AJ, 112, 1335
Wright, C. W. & Brainerd, T. G. 2000, ApJ, 534, 34
York, D. G. et al. 2000, AJ, 120, 1579
Zu, Y. & Mandelbaum, R. 2015, MNRAS, 454, 1161